Analysis of the Magnetic Properties of Ultra-thin Grain-oriented Silicon Steel and Fe-based Amorphous Alloy from Power Frequency to Intermediate Frequency

Guang Ma *, Ling Cheng *, Yu Han, Chengxu He

Posted Date: 22 March 2024

doi: 10.20944/preprints202403.1290.v1

Keywords: Ultra-thin grain-oriented silicon steel; Fe-based amorphous alloy; Epstein square ring; finite element method; loss

Article

Analysis of the Magnetic Properties of Ultra-Thin Grain-Oriented Silicon Steel and Fe-Based Amorphous Alloy from Power Frequency to Intermediate Frequency

Guang Ma *, Ling Cheng *, YU Han and Chengxu He

State Key Laboratory of Advanced Power Transmission Technology (State Grid Smart Grid Research Institute Co., Ltd), Changping District, Beijing 102209, China

* Correspondence: G.M. (maguang@geiri.sgcc.com.cn; Tel.: 010-66601570) and L.C. (chengling1107@126.com; Tel.: 010-66601563)

Abstract: The magnetic properties of 0.10 mm ultra-thin grain-oriented (UTGO) silicon steel and Fe-based amorphous (FBA) alloy under sinusoidal excitation were measured experimentally, and the magnetic field strength and iron loss of the two materials under different frequencies and magnetic densities were obtained. Based on the measured data, the magnetization and loss characteristics of the two materials were analyzed and compared. Furthermore, two Epstein square ring models of the same specification and different materials were designed, and the reliability of the models was verified. Then, the electromagnetic characteristics of the two Epstein square ring models at higher and lower frequencies were calculated by using the finite element method, and the iron loss was obtained and compared. The results show that the FBA alloy has good application characteristics at low frequency and low power, and the 0.10 mm UTGO silicon steel has good application characteristics at high frequency and high power. This research can provide important data basis to promote the application of these two materials in new energy equipment.

Keywords: ultra-thin grain-oriented silicon steel; Fe-based amorphous alloy; Epstein square ring; finite element method; loss

1. Introduction

The vigorous development of clean energy presents the traditional AC distribution network with the challenge of more and more DC power supply, DC load and diversified power demand. The electric energy produced by wind and solar generation units cannot be directly fed into the AC power grid, especially for offshore wind farms located far offshore; a converter platform with high efficiency and high reliability to collect and transmit the electric energy produced by wind turbines is essential [1]. By using a dedicated DC-DC converter at the output of each wind turbine, in a modular parallel or series manner, a more economical high voltage direct current transmission system can be achieved. Due to the progress of power semiconductors, magnetic materials and advanced control methods, power electronic transformers with isolated medium and high frequency transformers as core components have been rapidly promoted in industrial applications of wind power, photovoltaic and other new energy conversion systems [2]. Taking the wind power generation system as an example, as an electric energy conversion device, the high-frequency transformer primary side converter converts the power frequency AC electric energy produced by the wind generator into high-frequency square wave signals, and the subside converter restores the high-frequency square wave signals into power frequency AC electric energy for the subordinate power equipment [3]. The intermediate DC link in the Power Electronic Transformer (PET) can be used as a port for large-scale distributed power generation systems, energy storage systems, and DC loads such as electric vehicles to connect to the grid. The most significant difference between PET in wind power generation

 doi:10.20944/preprints202403.1290.v1

equipment and 50 Hz power frequency transformers is the higher operating frequency, usually in the range of a few kHz to tens of kHz [4]. Therefore, the bulky magnetic components in the traditional power transformer can be replaced by lighter-weight and smaller high-frequency magnetic cores, which can save the amount of transformer metal materials, reduce the manufacturing cost of the transformer, and thereby effectively improve the power density of the device. PET's advantages in work efficiency and controllability also provide an effective guarantee for the efficient operation of wind power transmission and distribution systems. In wind farms, the installation platform of distribution stations is usually indispensable for traditional power transformers, while high-frequency transformers can be installed either in the engine room or in the base of wind turbines due to their advantages in volume and weight, eliminating the need for bulky large substation platforms, and improving the excellent performance of wind turbines in terms of cost, design and maintenance [5,6].

A medium- and high-frequency transformer is the core equipment of a power electronic transformers; with increasing frequency, the loss of the medium- and high-frequency transformer core will be higher and higher, resulting in higher and higher temperature rise of power equipment and damage, shorten the service life. The loss characteristics between different magnetic materials will be different, in the process of designing power equipment, it is necessary to consider the influence of the core magnetic material properties. A new permanent magnet linear synchronous motor structure using oriented silicon steel sheet instead of the traditional non-oriented silicon steel sheet as the moving core material has been proposed, which improves the electromagnetic thrust and overload capacity [7]. The use of grain-oriented silicon steel in axial flux permanent magnet machines improves its torque and efficiency, and highlights the advantages of grain-oriented silicon steel in the application of yokeless stator axial flux permanent magnet (AFPM) machines [8]. By using three test motors, one made of conventional steel, high-silicon steel and amorphous iron [9], it is proved that magnetostriction has a significant effect on amorphous iron, but almost negligible effect on high-silicon steel. Considering the use of high-silicon steel instead of amorphous metal as a rotor to improve mechanical strength without affecting the performance of the motor proves the feasibility of high-silicon steel as a rotor and its potential for large-scale production [10]. The performance of a multistage axial flux permanent magnet motor with different stator core materials has been proposed and analyzed, and the difference in application performance of the three materials has been compared [11]. Comparative analysis, prototyping and testing of two kinds of surface mount permanent magnet synchronous motors (PMSMs) with the same physical size but different stator core materials were carried out, and it was found that the additive PMSM has very low no-load iron loss characteristics [12]. The influence of 6.5% silicon steel and cobalt-ferroalloy, two soft magnetic materials, on the design of high-speed machines is studied [13]. Therefore, the manufacture of new materials and the exploration of magnetic properties of different magnetic materials are of great significance for their application in power equipment.

In this work, Epstein square ring is used to measure the magnetic properties of 0.10 mm UTGO silicon steel at different frequencies, and the magnetic properties are compared with those of FBA alloy s at different frequencies. Then, COMSOL finite element calculation software is used to simulate the Epstein square ring. Based on the electromagnetic characteristics of 0.10 mm UTGO silicon steel and FBA alloy magnetic materials, the core magnetic field distribution and loss of the Epstein square ring of the two magnetic materials are calculated and analyzed at higher and lower frequencies, and the analyses are compared.

2. Experimental Measurment System

Many scholars and engineers attach great importance to the measurement method of electromagnetic properties of magnetic materials. At present, there are basically three kinds of measurement methods: the single slice measurement method, the standard Epstein square ring method, and the ring sample method [14–18]. Among them, the more traditional measurement methods are the Epstein square ring method and the ring sample method. The basic composition principle of Epstein square circle measurement method is to form a box of silicon steel sheets by

 doi:10.20944/preprints202403.1290.v1

double tower joints, form four beams with equal length and cross section, and insert them into four coils. We used the Brockhaus MPG-200D soft magnetic measurement system (including arbitrary waveform generator, power amplifier, control program, etc.) from the German BROCKHAUS MEASUREMENTS company to complete the test of the square ring sample. The Epstein square coil consists of a primary coil (magnetization winding) in the outer layer, a secondary coil (induction voltage winding) in the inner layer, and a sample as a core [19]. A physical diagram of the Epstein square ring is shown in Figure 1.

Figure 1. Epstein square ring.

The 0.10 mm UTGO silicon steel was selected as the research object, and the magnetic field strength and loss value of the magnetic material were measured by Epstein square ring method at 0.1 T-1.7 T under sinusoidal excitation. The sample size is 300 mm×30 mm, and the number of primary- and secondary-side turns is 100. An experimental schematic diagram is shown in Figure 2. After obtaining the measurement results, the electromagnetic properties of the FBA alloy materials measured by the ring sample method are compared.

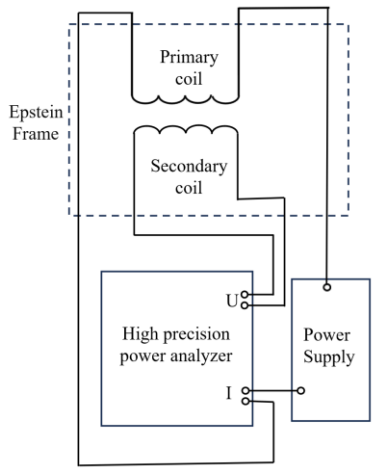

Figure 2. Schematic diagram of the experiment.

3. Measurement Results

3.1. Magnetization Curve Measurement Results

By comparing the magnetic properties of different silicon magnetic materials under different frequency sinusoidal magnetization conditions, the selection suggestions of different types of

 doi:10.20944/preprints202403.1290.v1

magnetic materials under different operating conditions can be given, which provides data support for the design of power electronic equipment [20].

Figure 3 shows the magnetization curve of 0.10 mm UTGO silicon steel and FBA alloy. It can be seen from the figure that the magnetization curve of 0.10 mm UTGO silicon steel tends to be saturated when the magnetic induction intensity is 1.6 T and the magnetic field intensity is about 80 A/m. The magnetization curve of the FBA alloy tends to be saturated when the magnetic field intensity is about 28.5 A/m and 1.4 T. Thus, 0.10 mm UTGO silicon steel has a high saturation magnetic induction strength and permeability, whereas the FBA alloy has low saturation magnetic induction strength and permeability. With an increase in frequency, the permeability of 0.10 mm UTGO silicon steel and FBA alloy decreases.

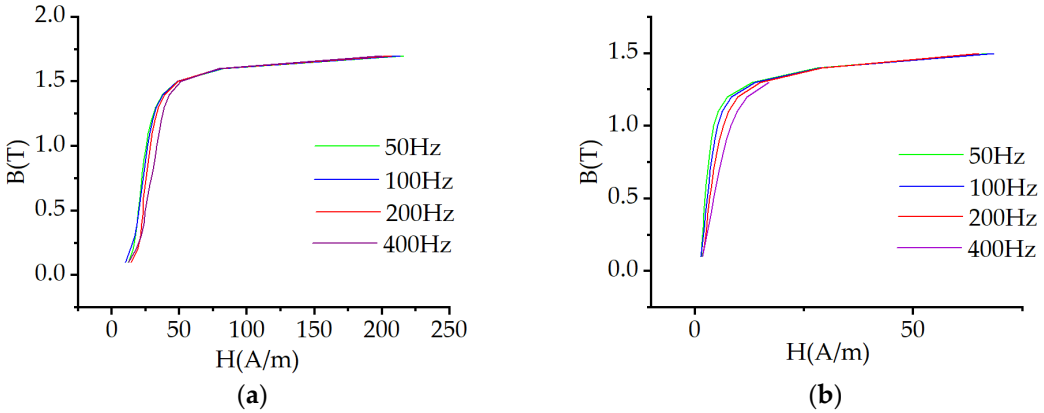

Figure 3. Magnetization curve: (**a**) 0.10 mm UTGO silicon steel magnetization curve; (**b**) FBA alloy magnetization curve.

3.2. Measurement Results of Loss Characteristics at Lower Frequencies

In order to facilitate observation and comparison, this paper classifies 50Hz-100Hz as low frequency and 200Hz-400Hz as high frequency. Figure 4 shows the loss characteristics of 0.10 mm UTGO silicon steel and FBA alloy at 50 Hz-100 Hz.

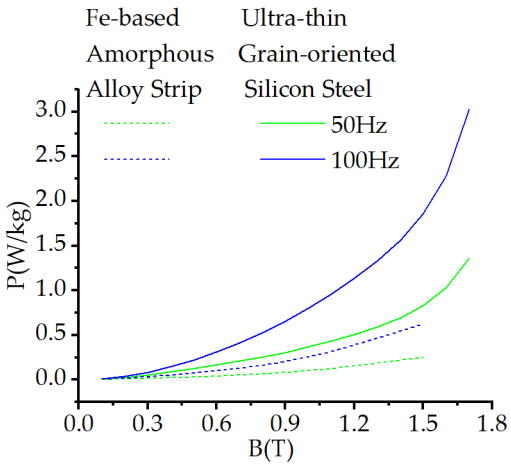

Figure 4. Loss characteristics at low frequency.

It can be seen from the figure that the loss curve of FBA alloy at 50 Hz-100 Hz is lower than that of 0.10 mm UTGO silicon steel at 50 Hz. In the range of 0.1 T-1.0 T, the loss curve of FBA alloy in 50 Hz-100 Hz and the loss curve of 0.10 mm UTGO silicon steel in 50 Hz-100 Hz are relatively gentle, while the loss curve of 0.10 mm UTGO silicon steel increases rapidly after 1.5 T. The iron loss density of 0.10 mm UTGO silicon steel is 1.03 W/kg when the frequency is 50 Hz and the magnetic induction

 doi:10.20944/preprints202403.1290.v1

intensity is 1.6 T, and the iron loss density is 0.37 W/kg when the magnetic induction intensity is 1.0 T. The iron loss density of FBA alloy is 0.25 W/kg when the frequency is 50 Hz and the magnetic induction intensity is 1.5 T, and the iron loss density is 0.10 W / kg when the magnetic induction intensity is 1.0 T. The loss density of 0.10 mm UTGO silicon steel at 50 Hz is higher than that of 0.18 mm oriented silicon steel [21].

3.3. Measurement Results of Loss Characteristics at Higher Frequencies

Figure 5 shows the loss characteristics of 0.10 mm UTGO silicon steel and FBA alloy at 200 Hz-400 Hz.

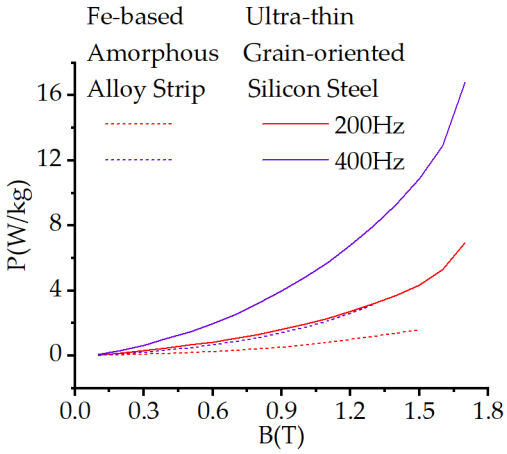

Figure 5. Loss characteristics at high frequency.

It can be seen from the diagram that in the high frequency range, the loss difference between 0.10 mm UTGO silicon steel and FBA alloy is more obvious. With the increase in frequency, the growth rate of the loss curve of 0.10 mm UTGO silicon steel is greater than that of FBA alloy. When the frequency is 200 Hz and the magnetic induction intensity is 1.0 T, the iron loss density of 0.10 mm UTGO silicon steel is 1.95 W / kg, and the iron loss density of FBA alloy is 0.66 W / kg. When the frequency is 400 Hz and the magnetic induction intensity is 1.0 T, the iron loss density of 0.10 mm UTGO silicon steel is 4.81 W/kg, and the iron loss density of FBA alloy is 1.75 W/kg.

The loss characteristics of FBA alloy at 200 Hz are lower than that of 0.10 mm UTGO silicon steel at 100 Hz, and higher than that of 0.10 mm UTGO silicon steel at 50 Hz. The change rate of the loss curve of 0.10 mm UTGO silicon steel at 200 Hz increases rapidly. With the increase of frequency, the loss of 0.10 mm UTGO silicon steel and FBA alloy increases, and the increase is the largest between 100 Hz and 200 Hz.

It can be seen from the above that 0.10 mm UTGO silicon steel has lower loss at high frequency and has better high frequency magnetic characteristics. The magnetic properties of FBA alloys have the lowest loss at both low frequency and high frequency and have the best magnetic properties.

4. Establishment of the Model

From the above analysis, it can be seen that 0.10 mm UTGO silicon steel has a high saturation magnetic induction strength and permeability; if applied to power equipment, it can reduce the volume of power equipment and achieve miniaturization. FBA alloys have lower losses at high frequencies and can also achieve miniaturization of power equipment. Therefore, in order to ensure that the application performance of the two materials can be compared, two Epstein square rings of the same specification are designed in this research to analyze and compare the magnetic characteristics of 0.10 mm UTGO silicon steel and FBA alloy at higher and lower frequencies.

 doi:10.20944/preprints202403.1290.v1

4.1. Structural Parameters of Epstein Square Ring

In order to compare and analyze the application performance of 0.10 mm UTGO silicon steel and FBA alloy in the same specification of power equipment, two kinds of Epstein square rings with the same design parameters were designed based on the above measured electromagnetic characteristic curves. In order to ensure the feasibility of the method, we use the Epstein square rings when measuring 0.10 mm UTGO silicon steel to build a model and verify the reliability of the model. The main design parameters are shown in Table 1. In medium frequency operation, the main magnetic flux density should not be close to the saturation magnetic flux density, and the magnetic flux far away from the saturation point is selected as the working magnetic density; so, the working magnetic flux is selected as 1.0 T.

Table 1. Main design parameters of 0.10 mm UTGO silicon steel Epstein square rings.

Outer perimeter	Inner perimeter	Magnetic circuit	N1	N2
280 mm	220 mm	940 mm	100	100

4.2. Computation Model

4.2.1. Electromagnetic Field Calculation Model

The finite element analysis software COMSOL is used to simulate the Epstein square coil, and the transient field is used to simulate the electromagnetic characteristics of the Epstein square coil. The following assumptions are made before calculation: the core, winding and other materials are isotropic; the influence of lead current and displacement current on the magnetic field is not considered. There is no free charge in the Epstein frame. The mathematical calculation method of Epstein square ring is used for the electromagnetic field; so, the equations involved are as follows.

$$\nabla \times \boldsymbol{H} = \boldsymbol{J} \tag{1}$$

$$\boldsymbol{B} = \nabla \times \boldsymbol{A} \tag{2}$$

$$\boldsymbol{J} = \sigma \boldsymbol{E} + \boldsymbol{J_e} \tag{3}$$

$$\boldsymbol{E} = -\frac{\partial \boldsymbol{A}}{\partial \mathrm{t}} \tag{4}$$

The constitutive relation of the equation is

$$\boldsymbol{B} = \mu \boldsymbol{H} \tag{5}$$

According to formulas (1) - (5), the vector magnetic potential equation of the magnetic field of the Epstein square ring is derived as follows:

$$\frac{1}{\mu}\left(\frac{\partial^2 \boldsymbol{A}}{\partial x^2} + \frac{\partial^2 \boldsymbol{A}}{\partial y^2} + \frac{\partial^2 \boldsymbol{A}}{\partial z^2}\right) = -\sigma \frac{\partial \boldsymbol{A}}{\partial t} + \boldsymbol{J_e} \tag{6}$$

where $\boldsymbol{B}$ represents the magnetic induction intensity vector; $\boldsymbol{H}$ represents the magnetic field intensity vector; $\boldsymbol{E}$ denotes the electric field intensity vector; $\boldsymbol{A}$ represents the vector magnetic potential; $\boldsymbol{J}$ represents the current density; $\boldsymbol{J}_e$ represents the external current density; σ is the conductivity; μ is the permeability.

4.2.2. Loss Calculation Model

Although it is very desirable to reduce the volume of power equipment by increasing the frequency, the higher the operating frequency, the smaller the volume, the smaller the surface area that can be used for heat dissipation, and the rapid increase in the high frequency loss of the core and winding, resulting in low power transmission efficiency [22,23]. Therefore, it is necessary to calculate and analyze the loss.

 doi:10.20944/preprints202403.1290.v1

There are two main methods for calculating the core loss under sinusoidal excitation, namely, the iron loss separation method and the Steinmetz empirical formula method. According to the different mechanisms of magnetic core loss, the Bertotti iron loss separation method decomposes the magnetic core loss into hysteresis loss, eddy current loss and residual loss. The calculation formula of the iron loss separation method under sinusoidal excitation is

$$P_V = P_h + P_e + P_c = k_h B_m^{\alpha} f + k_e B_m^2 f^2 + k_c B_m^{1.5} f^{1.5} \quad (7)$$

Among them, P_V is the total loss, k_h is the hysteresis loss coefficient, k_e is the eddy current loss coefficient, k_c is the residual loss coefficient, and α is the magnetic density coefficient.

Generally, as long as the magnetic core loss data measured experimentally under sinusoidal excitation are fitted, the magnetic core loss coefficient and the magnetic flux density index value can be obtained, and then the analytical calculation formula of the iron loss separation method can be obtained.

As the saturation degree increases, the hysteresis loop will produce a local hysteresis loop, which will increase the hysteresis loss. If the coefficient α is fitted with only one constant, the error between the fitting value of hysteresis loss and the measured value will increase when the peak value of magnetic induction intensity Bm is higher. And the hysteresis loss Ph is the energy loss caused by the magnetic domain overcoming the field force during the rotation process. Its size depends on the amplitude Bm of the magnetic flux density and is independent of the frequency f of the external excitation [24]. Therefore, we express α in the form of Bm polynomial [25], namely,

$$\alpha(B_m) = \alpha_3 B_m^3 + \alpha_2 B_m^2 + \alpha_1 B_m + \alpha_0 \quad (8)$$

In the formula, α_i(i=0,1,2,3) is the coefficient of the i-th power of B_m, and α_i is obtained by fitting the measured values.

The hysteresis loss formula can be obtained as

$$P_h = k_h B_m^{(\alpha_3 B_m^3 + \alpha_2 B_m^2 + \alpha_1 B_m + \alpha_0)} f \quad (9)$$

The coefficient of hysteresis loss of 0.10 mm UTGO silicon steel and FBA alloy can be obtained by the least square method, as shown in Table 2.

Table 2. Coefficient of hysteresis loss.

	FBA alloy	0.10 mm UTGO silicon steel
k_h	**0.0016**	**0.00686**
α_0	**1.30**	**1.65**
α_1	**0.61**	**0**
α_2	**0.55**	**-1.01**
α_3	**-0.40**	**0.74**

At this time, the total loss PV is

$$P_V = k_h B_m^{(\alpha_3 B_m^3 + \alpha_2 B_m^2 + \alpha_1 B_m + \alpha_0)} f + k_e B_m^2 f^2 + k_c B_m^{1.5} f^{1.5} \quad (10)$$

4.3. Finite Element Calculation Model

The finite element model of this paper is an idealized three-dimensional model, which focuses on calculating the flux and loss of the magnetic material surrounded by the coil. The loss is mainly concentrated on the magnetic material surrounded by the coil, and the loss at the corner is extremely low, so the error is within the controllable range. Firstly, the three-dimensional model of Epstein frame is established according to the design parameters in the finite element calculation software COMSOL. The magnetic properties of 0.10 mm ultra-thin silicon steel sheet and amorphous alloy measured above are added to the three-dimensional model, including magnetization curve and density. The magnetic field physical field interface is added to combine the calculation model with

 doi:10.20944/preprints202403.1290.v1

the three-dimensional model of Epstein frame, and the corresponding excitation is applied to the coil, and the model is meshed.

5. Results and Discussion

In order to make the electromagnetic properties of 0.10 mm UTGO silicon steel and FBA alloy more intuitive and reliable, this work uses the same specification of Epstein square ring to compare and analyze the electromagnetic properties of 0.10 mm UTGO silicon steel and FBA alloy.

5.1. Magnetic Flux Density Cloud of Epstein Square Ring

In order to analyze the distribution of magnetic flux density in the Epstein frame more intuitively, this paper obtains the magnetic flux density distribution of FBA alloy and 0.10 mm UTGO silicon steel Epstein frame at different frequencies when the magnetic flux density is 1.0 T and 1.2 T, as shown in Figures 6–9.

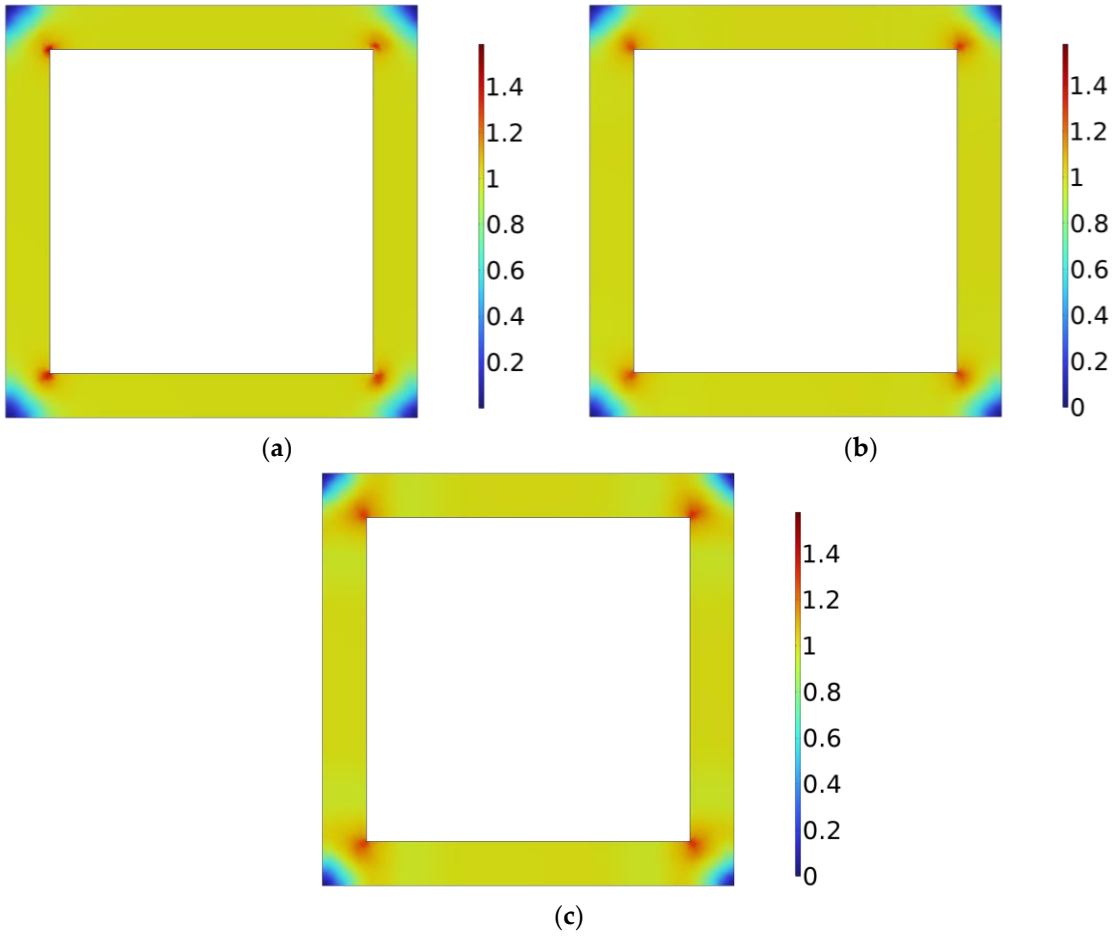

Figure 6. Cloud map of the magnetic flux density of FBA alloy at 1.0 T: (a) 50 Hz; (b) 200 Hz;(c) 400 Hz.

 doi:10.20944/preprints202403.1290.v1

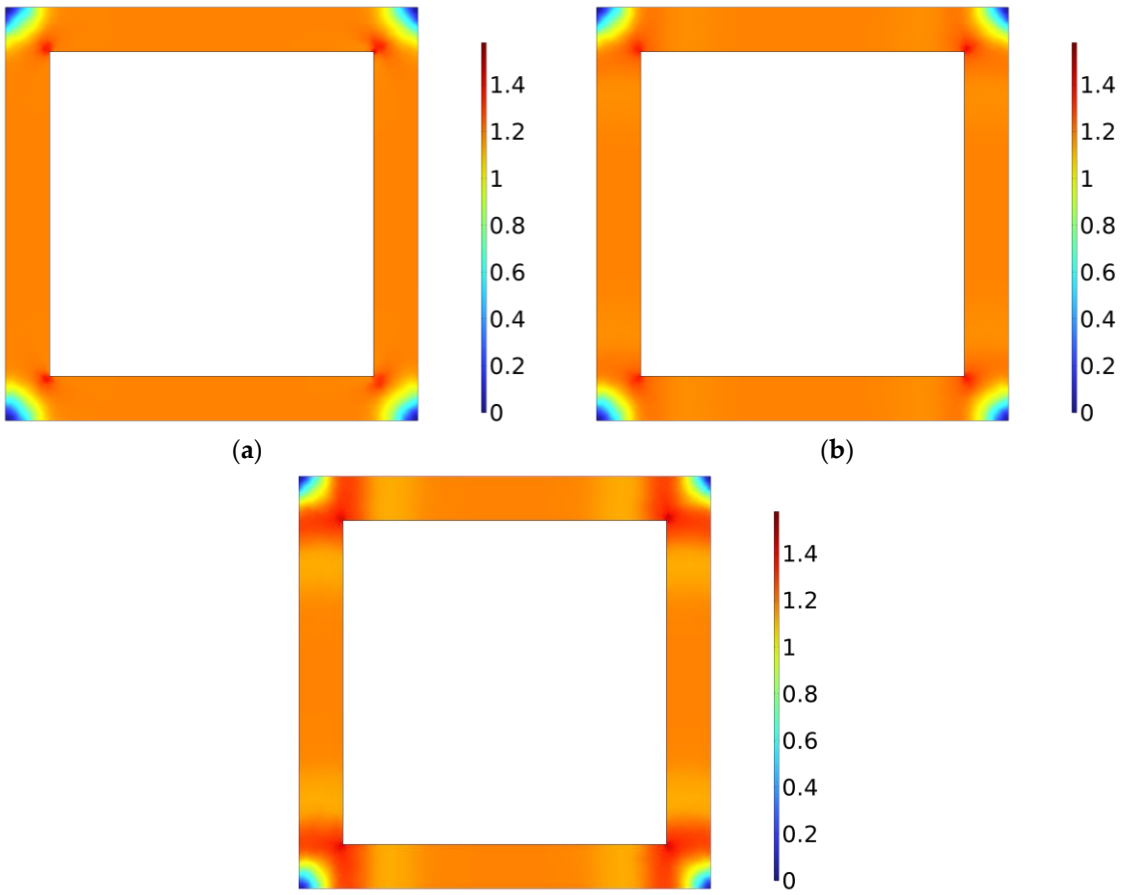

Figure 7. Cloud map of the magnetic flux density of FBA alloy at 1.2 T: (a) 50 Hz; (b) 200 Hz;(c) 400 Hz.

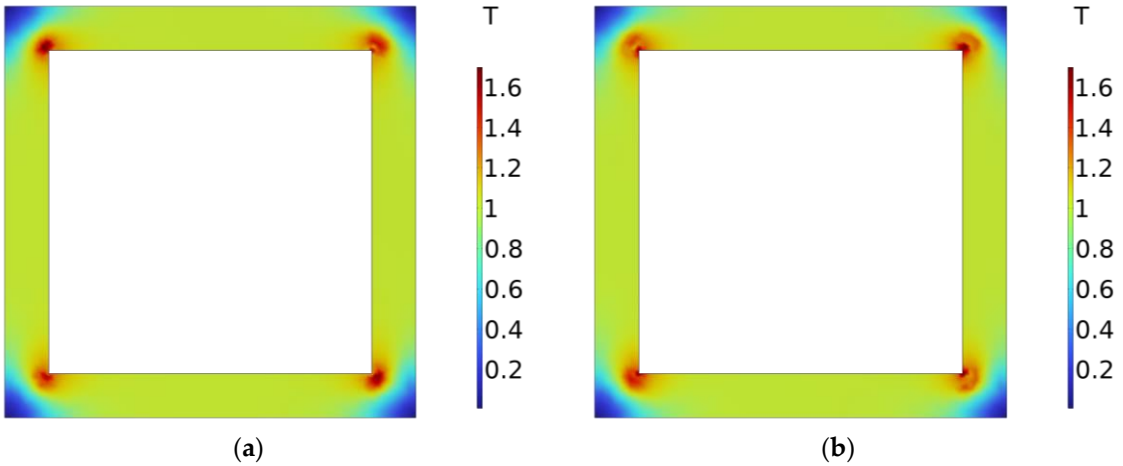

 doi:10.20944/preprints202403.1290.v1

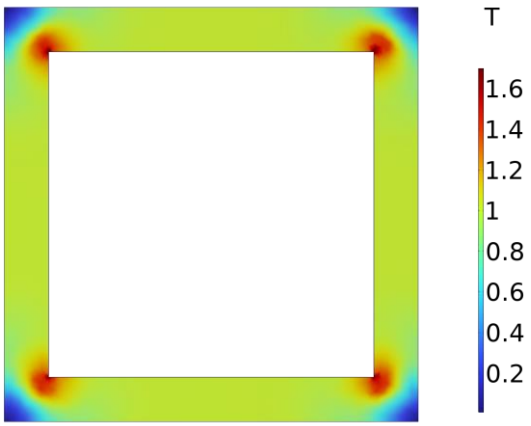

(**c**)

Figure 8. Cloud image of the magnetic flux density of 0.10 mm UTGO steel at 1.0 T: (a) 50 Hz; (b) 200 Hz;(c) 400 Hz.

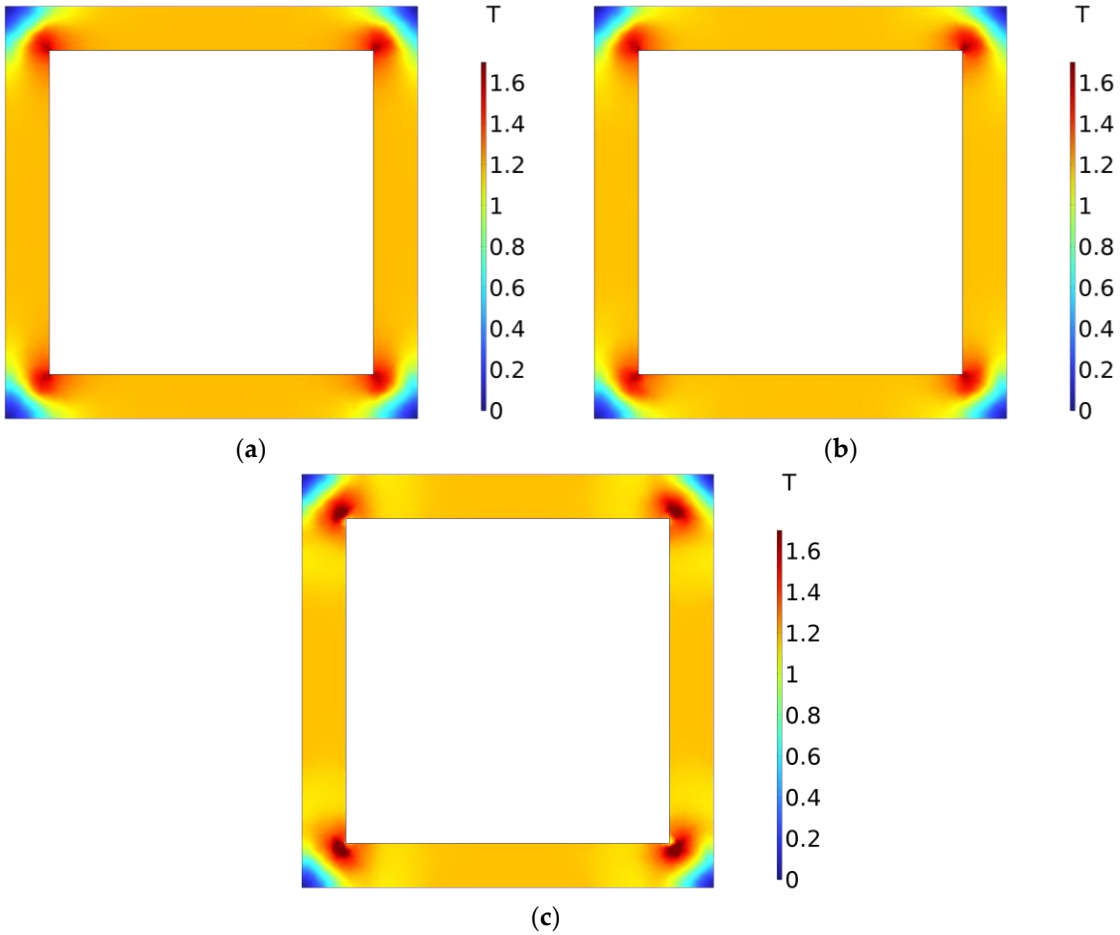

(**a**) (**b**)

(**c**)

Figure 9. Cloud image of the magnetic flux density of 0.10 mm UTGO steel at 1.2 T : (a) 50 Hz; (b) 200 Hz;(c) 400 Hz.

It can be seen from the diagram that the magnetic density distribution of Epstein square rings on each side is the same and uniform, and the magnetic flux density is high and unevenly distributed only at the corner. With the increase in frequency, the magnetic flux density at the corner of Epstein 's square circle also increases significantly, and the magnetic flux density at other locations except the corner remains unchanged. At the same frequency, the magnetic induction intensity at the corner of 0.10 mm UTGO silicon steel Epstein square ring is higher than that of FBA alloy Epstein square ring.

 doi:10.20944/preprints202403.1290.v1

With the increase of the working magnetic flux density, the magnetic flux density at the corner of Epstein 's square circle also increases significantly and tends to be more saturated.

5.2. Epstein square ring loss calculation results

5.2.1. Epstein Square Circle Loss Cloud Map

Similarly, in order to analyze the distribution of loss in Epstein frame more intuitively, this paper obtains the loss distribution nephogram of FBA alloy and 0.10 mmUTGO silicon steel Epstein frame at different frequencies when the magnetic flux density is 1.0 T and 1.2 T, as shown in Figures 10–13. It can be seen from the diagram that the loss and magnetic density have the same distribution law. With the increase of frequency and magnetic flux density, the overall loss of Epstein frame increases, and the loss at the corner is significantly higher than that at other positions. The loss at other positions except the corner remains evenly distributed. At the same frequency and magnetic flux density, the loss of 0.10 mm UTGO silicon steel Epstein frame is higher than that of FBA alloy Epstein frame.

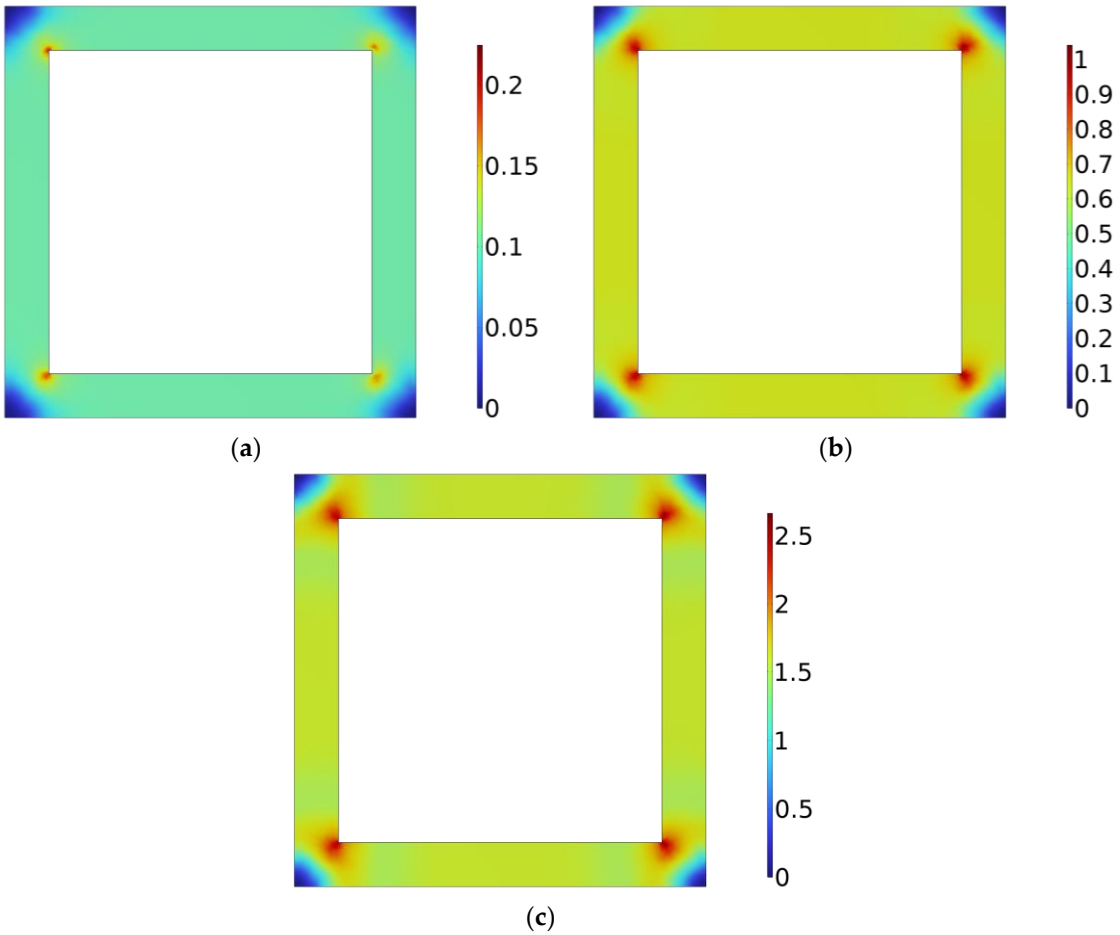

Figure 10. Cloud map of the loss of FBA alloy: (a) 50 Hz; (b) 200 Hz; (c) 400 Hz.

 doi:10.20944/preprints202403.1290.v1

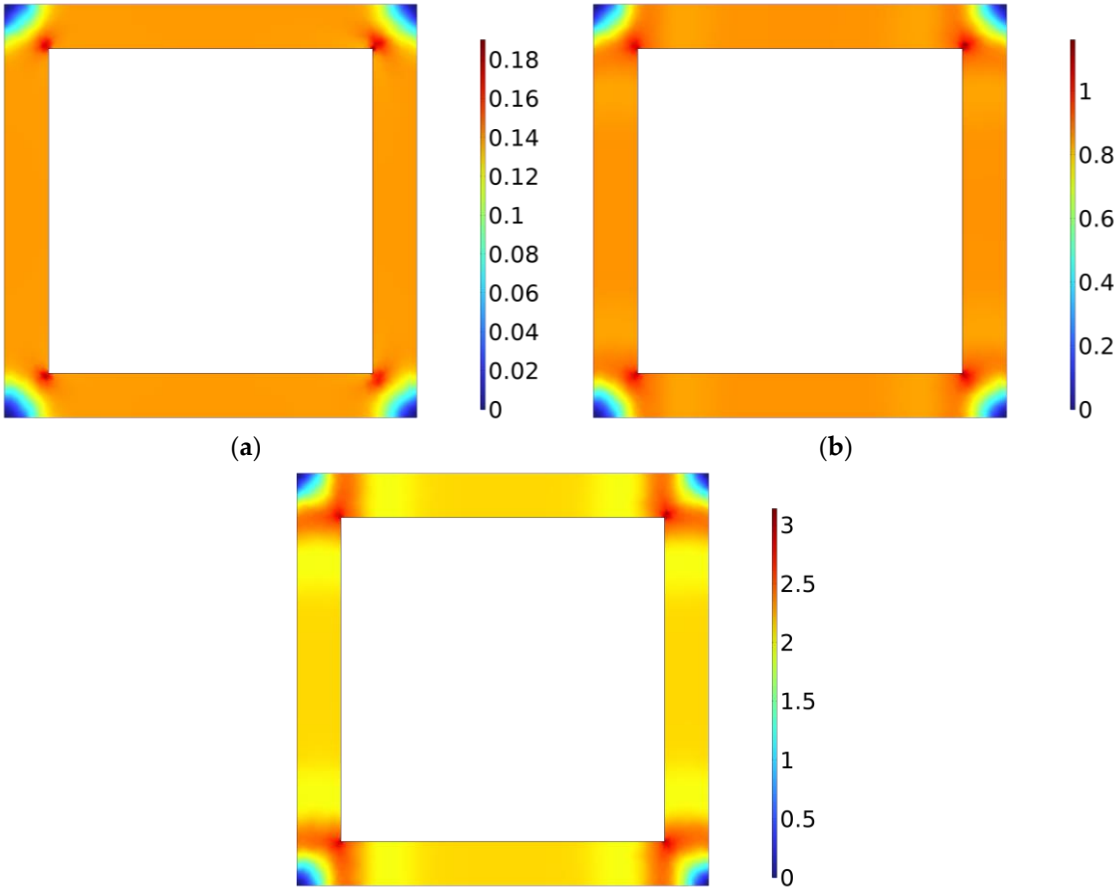

Figure 11. Cloud map of the loss of FBA alloy: (a) 50 Hz; (b) 200 Hz; (c) 400 Hz.

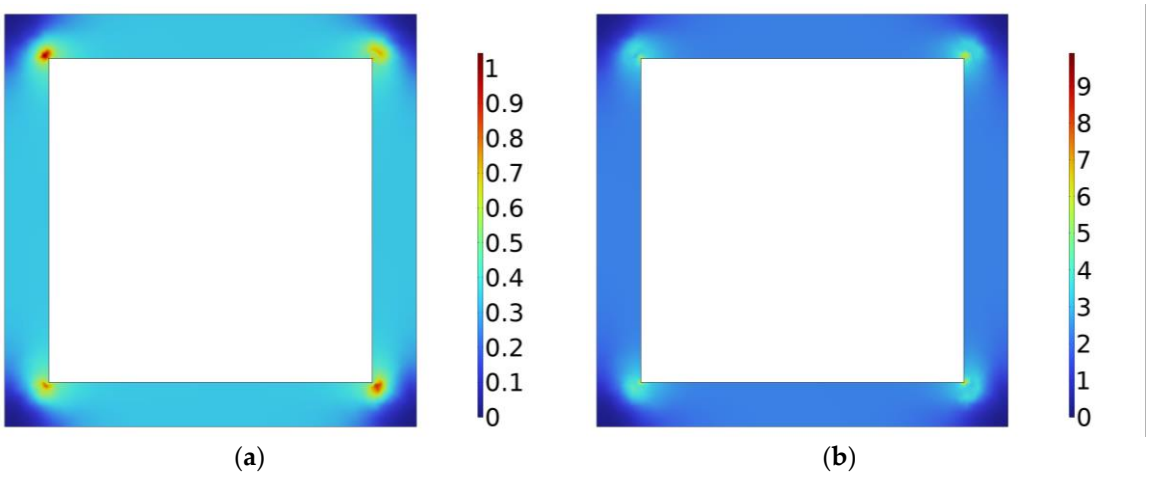

 doi:10.20944/preprints202403.1290.v1

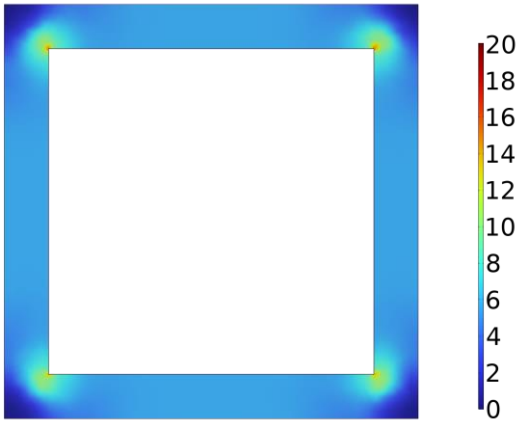

(**c**)

Figure 12. Cloud image of the loss of 0.10 mm UTGO steel: (a) 50 Hz; (b) 200 Hz; (c) 400 Hz.

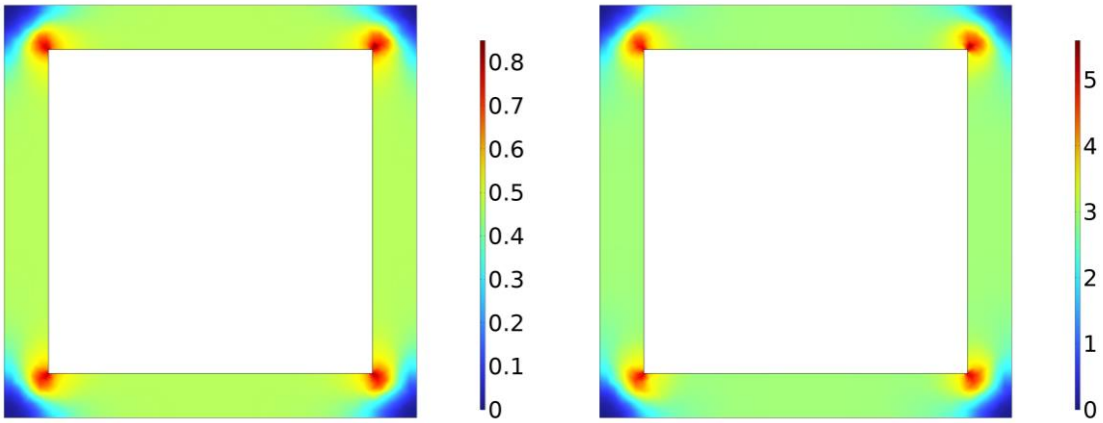

(**a**) (**b**)

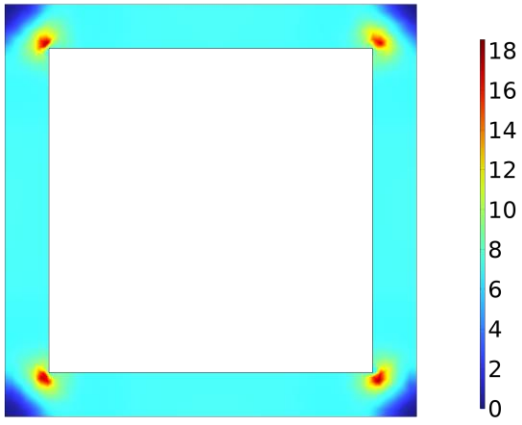

(**c**)

Figure 13. Cloud image of the loss of 0.10 mm UTGO steel: (a) 50 Hz; (b) 200 Hz; (c) 400 Hz.

5.2.2. Comparison between the Calculated Value of the Epstein Square Ring Loss and the Experimental Value

Calculate the specific gravity loss of epstein square ring, the calculation formula is as follows:

$$P_V = \sum_{i=1}^{n} p_i/m = \frac{\int pdV}{\mathrm{m}} \tag{11}$$

Among them, p_i is the loss of Epstein square circle under the i th calculation unit, and m is the mass of Epstein square circle.

 doi:10.20944/preprints202403.1290.v1

The magnetic properties of 0.10 mm UTGO silicon steel are measured by using the Epstein square ring method; so, the electromagnetic properties of 0.10 mm UTGO steel are calculated first.

As shown in Figure 14, the calculated values of the Epstein square loop loss curve with 0.10 mm UTGO steel were compared with the experimental values at 50 Hz, 200 Hz and 400 Hz frequencies. It can be seen from the figure that the error between the calculated value and the experimental value of the mathematical model of the electromagnetic characteristics of the 0.10mm UTGO steel Epstein square ring with a frequency of 50Hz is generally large in the range of 0.1T-1.5T, and the maximum error is 9.53 %. The maximum error between the calculated value and the experimental value of the mathematical model of the electromagnetic characteristics of the 0.10mm UTGO steel Epstein square ring with a frequency of 200Hz is 9.87 % in the range of 0.1T-1.5T, and the maximum error in the range of 0.7T-1.5T magnetic flux density is 3.86 %. The error between the calculated value and the experimental value of the mathematical model of the electromagnetic characteristics of the Epstein square ring with a frequency of 400 Hz is small in the range of 0.1 T-1.5 T. In the magnetic flux density range of 0.1 T-0.4 T, the error is relatively large, and the maximum deviation is 8.87 %. In the range of 0.4 T-1.5 T magnetic flux density, the error is relatively small, and the maximum error is 4.65 %.

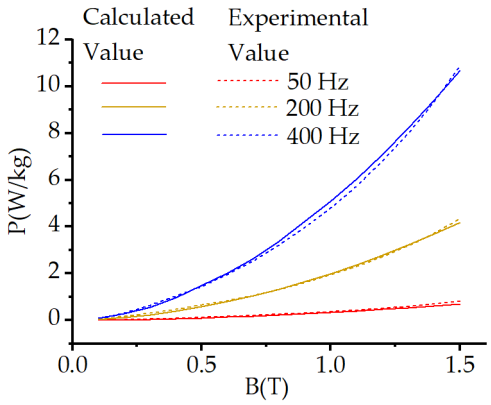

Figure 14. Comparison of the calculated and experimental values of the Epstein frame loss of 0.10 mm UTGO silicon steel.

Figure 15 shows the comparison between the calculated and experimental values of the loss curves of the Epstein square ring using FBA alloy at 50 Hz, 200 Hz and 400 Hz.

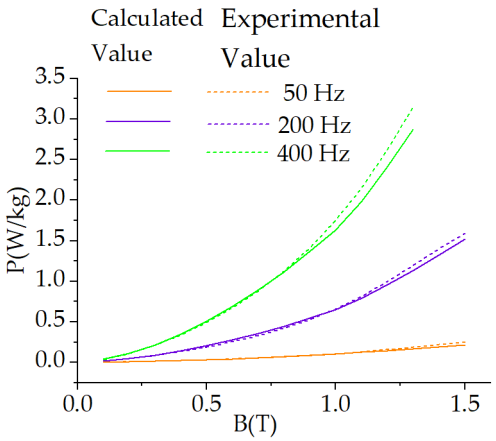

Figure 15. Comparison of the calculated and experimental values of the Epstein frame loss of the FBA alloy.

It can be seen from Figure 15 that in the range of 0.1-0.4T magnetic induction intensity, the error between the calculated value of the mathematical model of the electromagnetic characteristics of the

 doi:10.20944/preprints202403.1290.v1

FBA alloy Epstein square ring with a frequency of 50Hz and the experimental value is relatively small, and the maximum error is 3.14 %. In the range of 0.5-1.5 T magnetic flux density, the error is large, and the maximum error is 8.62 %. The error between the calculated value and the experimental value of the mathematical model of the electromagnetic characteristics of the Epstein square ring of the FBA alloy with a frequency of 200Hz is 8.12 % in the range of 0.1T-1.5T. The error between the calculated value of the mathematical model and the experimental value of the electromagnetic characteristics of the FBA alloy Epstein square coil with a frequency of 400 Hz in the range of 0.1 T-0.9 T magnetic flux density is relatively small, and the maximum error is 4.40 %. The error is large in the range of 1.0-1.3 T magnetic flux density, and the maximum error is 8.81 %.

It can be seen from the above results that the mathematical models of electromagnetic properties adopted by different magnetic materials will be affected by nonlinearity and produce large errors. Especially under the condition of high frequency and high flux, the smaller hysteresis loop further increases the influence of nonlinearity. The established calculation model of electromagnetic characteristics can effectively complete the calculation of magnetic field and loss of Epstein frame within the allowable error range.

6. Conclusion

In this paper, the magnetic field strength and iron loss of 0.10 mm UTGO silicon steel and FBA alloy under different magnetic induction intensities at high and low frequencies were measured and analyzed by experiments and calculations.

In the frequency range of 50 Hz-400 Hz, the saturation magnetic induction intensity of 0.10 mm UTGO silicon steel is higher and the loss is also higher. FBA alloy has the lowest saturation magnetic induction and low loss. Due to the brittleness of FBA alloy, it has great potential in low frequency and low power applications. Although the loss characteristics of 0.10 mm UTGO silicon steel at high frequency are not as low as that of FBA alloy, it has good mechanical strength and can realize the application performance of high frequency and high power.

When calculating the electromagnetic characteristics, the established calculation model can effectively complete the calculation of the electromagnetic characteristics of Epstein 's square coil.

Author Contributions: Conceptualization, G.M. and L.C.; methodology, L.C. and Y.H.; software, L.C. and C.H.; validation, G.M., L.C., and C.H.; formal analysis, L.C.; investigation, L.C. and C.H.; resources, L.C.; data curation, L.C. and C.H.; writing—original draft preparation, L.C.; writing—review and editing, G.M.; visualization, C.H.; supervision, Y.H.; project administration, Y.H.; funding acquisition, Y.H. All authors have read and agreed to the published version of the manuscript.

Funding: This research was funded by the State Grid Corporation of China, grant number 5500-202258353A-2-0-SY.

Data Availability Statement: The data presented in this study are available in the article.

Conflicts of Interest: The authors declare that the research was conducted in the absence of any commercial or financial relationships that could be construed as a potential conflicts of interest.

References

1. Elangovan, S. Recent trends in sustainable development of renewable energy. 2017 International Conference on Advances in Electrical Technology for Green Energy (ICAETGT), Coimbatore, India, 2017.
2. Ahmed, S. D.; Al-Ismail, F. S. M.; Shafiullah, M. Al-Sulaima, F. A.; El-Amin, I. M. Grid Integration Challenges of Wind Energy: A Review. *IEEE Access* **2020**, *8*, 10857-10878.
3. Sun, C.; Chen, J.; Tang Z. New Energy Wind Power Development Status and Future Trends. 2021 International Conference on Advanced Electrical Equipment and Reliable Operation (AEERO), Beijing, China, 2021.
4. Roasto, I.; Romero-Cadaval, E.; Martins, J.; Smolenski, R. State of the art of active power electronic transformers for smart grids. IECON 2012 - 38th Annual Conference on IEEE Industrial Electronics Society, Montreal, QC, Canada, 2012.

5. Sun, C.; Chen, J.; Tang, Z. New Energy Wind Power Development Status and Future Trends. 2021 International Conference on Advanced Electrical Equipment and Reliable Operation (AEERO), Beijing, China, 2021.
6. Zhu, L.; Zheng, H.; Ji, H.; Li, G.; Li, H.; S. Yao, Development Trends and Suggestions on Offshore Wind Power of China. 2021 IEEE Sustainable Power and Energy Conference (iSPEC), Nanjing, China, 2021.
7. Dong, T.; Fu, R., Zhang, B.; Peng, B.; Wei, X. Analysis of Permanent Magnet Linear Synchronous Motor made by Oriented Silicon Steel Sheet, 2021 13th International Symposium on Linear Drives for Industry Applications (LDIA), Wuhan, China, 2021.
8. Geng, W.; Hou, J.; Li, Q. Electromagnetic Analysis and Efficiency Improvement of Axial-Flux Permanent Magnet Motor With Yokeless Stator by Using Grain-Oriented Silicon Steel, *IEEE Transactions on Magnetics* **2022**, *58*, 1-5.
9. Sobue et al, H. Analysis and Experimental Comparison of Acoustic Noise of Three Switched Reluctance Motors Made of Conventional Steel, High Silicon Steel, and Amorphous Iron. *IEEE Transactions on Industry Applications* **2021**, *57*, 5907-5915.
10. Ou, J.; Liu, Y.; Breining, P.; Gietzelt, T.; Wunsch, T. Doppelbauer, M.; Experimental Characterization and Feasibility Study on High Mechanical Strength Electrical Steels for High-Speed Motors Application, *IEEE Transactions on Industry Applications* **2020**, *57*, 284-293
11. Sun, S.; Jiang, F.; Li, T.; Xu B.; Yang, K. Comparison of A Multi-Stage Axial Flux Permanent Magnet Machine With Different Stator Core Materials. *IEEE Transactions on Applied Superconductivity* **2020**, *30*, 1-6.
12. Tong, W.; Dai, S.; Wu S.; Tang, R. Performance Comparison Between an Amorphous Metal PMSM and a Silicon Steel PMSM, *IEEE Transactions on Magnetics* **2019**, *55*, 1-5.
13. Fernando, N.; Vakil, G.; Arumugam, P.; Amankwah, E; Gerada C.; Bozhko, S. Impact of Soft Magnetic Material on Design of High-Speed Permanent-Magnet Machines. *IEEE Transactions on Industrial Electronics* **2017**, *64*, 2415-2423.
14. Sato et al, Y. Accuracy Investigation of High-Frequency Core Loss Measurement for Low-Permeability Magnetic Materials. 2023 IEEE International Magnetic Conference - Short Papers (INTERMAG Short Papers), Sendai, Japan, 2023.
15. V. Ioniță, L. Petrescu; E. Cazacu, Coils-Based Measurement System for Soft Magnetic Materials, 2021 12th International Symposium on Advanced Topics in Electrical Engineering (ATEE), Bucharest, Romania, 2021
16. P. C. Sarker, Y. Guo, H. Y. Lu and J. G. Zhu, Measurement and Modeling of Rotational Core Loss of Fe-Based Amorphous Magnetic Material Under 2-D Magnetic Excitation, *IEEE Transactions on Magnetics* **2021**, *57*, 1-8
17. Wan, Z.; Liu, Z.; Yuan, W. Automated Measurement System for Hysteresis Lines and Magnetic Parameters of Magnetic Materials. 2021 IEEE Far East NDT New Technology & Application Forum (FENDT), Kunming, China, 2021.
18. Yang et al, M. "Magnetic Properties Measurement and Analysis of High Frequency Core Materials Considering Temperature Effect," *IEEE Transactions on Applied Superconductivity* **2020**, *30*, 1-5
19. Shilyashki, G.; Pfützner, H.; Giefing, M. Bengtsson, C. Giant Epstein Tester for Magnetic Energy Loss Measurements of Non-Annealed Domain-Refined Fe–Si. *IEEE Transactions on Magnetics* **2022**, *58*, 1-6.
20. Liu, Y.; Gong, X. H.; Chen, X. Measurement and Comparative Analysis of Magnetic Properties of 0.10 mm and 0.23 mm Oriented Silicon Steel under Different Operating Conditions, *China Electric Power* **2022**, ,*55 (02)*, 181-189.
21. Ling, C.; Guang, M.; Chao, H. Z. Analysis of Performance Simulation of Iron Core and Electromagnetic Characteristics of 0.18 mm Grain-oriented Silicon Steel with Ultra-low Loss. *Electrical steel* **2020**, *2 (01)*, 15-21.
22. Chen, J.; Hu, H.; Jiang, S.; Deng, L.; Peng, T.; Calculation of the Core Loss of High-Frequency High-Voltage Transformer Considering the Influence of Temperature. 2021 IEEE 4th Student Conference on Electric Machines and Systems (SCEMS), Huzhou, China, 2021.
23. Liu, X.; Zhao, L.; Ma, C.; Ge Q.; Li, Y. Optimization Simulation Analysis of Leakage Magnetic Field and Loss Characteristics of High Frequency Nanocrystalline Transformer. 2022 25th International Conference on Electrical Machines and Systems (ICEMS), Chiang Mai, Thailand, 2022.

 doi:10.20944/preprints202403.1290.v1

24. Yang et al., M. Application-oriented characterization and analysis of core materials under medium-frequency condition, *IEEE Trans. Power Electron*. **2023**, *38*, 11245-11259.
25. Gang, L.; Peng, S. L.; Gang, W. X.; Improvement and simulation application of core loss calculation method under sinusoidal and harmonic excitation. *Transactions of China Electrotechnical society* **2018**, *33(21)*, 4909-4918.